

Tunable Majorana corner modes in noncentrosymmetric superconductors: Tunneling spectroscopy and edge imperfections

S. Ikegaya¹, W. B. Rui², D. Manske¹ and Andreas P. Schnyder¹

¹ *Max-Planck-Institut für Festkörperforschung, Heisenbergstrasse 1, D-70569 Stuttgart, Germany*

² *Department of Physics and HKU-UCAS Joint Institute for Theoretical and Computational Physics at Hong Kong, The University of Hong Kong, Pokfulam Road, Hong Kong, China*

(Dated: October 11, 2021)

Majorana corner modes appearing in two-dimensional second-order topological superconductors have great potential applications for fault-tolerant topological quantum computations. We demonstrate that in the presence of an in-plane magnetic field two-dimensional $(s+p)$ -wave superconductors host Majorana corner modes, whose location can be manipulated by the direction of the magnetic field. In addition, we discuss the effects of edge imperfections on the Majorana corner modes. We describe how different edge shapes and edge disorder affect the number and controllability of the Majorana corner modes, which is of relevance for the implementation of topological quantum computations. We also discuss tunneling spectroscopy in the presence of the Majorana corner modes, where a lead-wire is attached to the corner of the noncentrosymmetric superconductor. The zero-bias differential conductance shows a distinct periodicity with respect to the direction of the magnetic field, which demonstrates the excellent controllability of the Majorana corner modes in this setup. Our results lay down the theoretical groundwork for observing and tuning Majorana corner modes in experiments on $(s+p)$ -wave superconductors.

I. INTRODUCTION

A central subject in physics of topological superconductivity [1–4] is the realization of fault-tolerant topological quantum computations [5–9] using Majorana zero modes [10–12]. So far, the existence of the Majorana zero modes has been experimentally demonstrated in various systems such as semiconductor-superconductor hybrids [13–24], magnetic atom chains on superconductors [25–28], and superconducting topological insulators [29–34]. However, to achieve the topological quantum computations, we have to manipulate the position of the Majorana zero modes for performing braiding operations, which is still a challenging task at the current stage.

Recently, a fresh route for realizing topological quantum computations has been discussed in the context of higher-order topological superconductivity [35–54]: a n th-order topological superconductor in d dimensions can host Majorana zero modes in $(d-n)$ dimensions for $n \geq 2$, whereas conventional topological superconductors correspond to the case with $n = 1$. Although the study of higher-order topological superconductors is still in its infancy, there have already been several theoretical predictions for two-dimensional second-order topological superconductors in which the position of emergent Majorana corner modes (MCMs) can be controlled by varying experimentally tunable parameters [48–54]. Moreover, braiding operations using the advantages of such tunable MCMs have been demonstrated theoretically [52–54]. Thus, this recent development in the physics of tunable MCMs shows great promise for the realization of fault-tolerant topological quantum computations.

A fundamental strategy for obtaining tunable MCMs is the application of magnetic fields to time-reversal invariant topological superconductors, which host helical Majorana edge states [38, 39, 48]. On the basis of

this strategy, the presence of tunable MCMs has been demonstrated in Rashba bilayers coupled to superconductors [50], semiconductor/iron-based superconductor hybrids [49], as well as spin-triplet helical p -wave superconductors [49, 53]. Even so, since these proposals have not yet been implemented experimentally, it is important to continue to propose alternative models hosting tunable MCMs. Thus, as the first objective of this paper, we demonstrate that a two-dimensional noncentrosymmetric $(s+p)$ -wave superconductor [55–61], which is experimentally realized, e.g., in CePt_3Si [62–69] or in CeRhSi_3 [70–73], can harbor the tunable MCMs by applying in-plane magnetic fields.

Moreover, while most previous studies on tunable MCMs consider square superconducting islands with clean edges, experimental implementations will most certainly deviate from such an ideal geometry. Thus, as the second objective of this paper, we study the effects of edge imperfections on the MCMs. For a square geometry with clean edges, we can find two stable Majorana zero modes. However, for more complicated edge configurations, the number of MCMs becomes more than two and depends on the applied magnetic field direction. In this case, we can no longer find a stable pair of Majorana zero modes that can make a full circle around the system, which complicates the braiding process. Thus, the edge configuration is an important factor for accomplishing the topological quantum computations in experiments.

At present, to the best of our knowledge, there are no specific theoretical proposals for detecting the tunable MCMs. Thus, as the third objective of this paper, we study the tunneling spectroscopy in the presence of the MCMs, where the normal lead wire is attached to the vicinity of the corner of the noncentrosymmetric superconductor. We demonstrate that the zero-bias conductance becomes a periodic function with respect to the di-

rection of the applied magnetic field. This characteristic periodicity is understood by the fact that the zero-bias conductance is enhanced only when the MCM exits at the corner connected with the lead wire. As a result, we propose a smoking-gun experiment for the detection of controllable MCMs.

The organization of this paper is as follows. In Sec. II, we first derive an effective edge theory describing the emergence of tunable MCMs in a noncentrosymmetric superconductor with in-plane magnetic fields. Then, we confirm the validity of the edge theory by employing numerical simulations on a two-dimensional tight-binding model. In Sec. III, we study the effects of edge imperfections on the tunable MCMs. Specifically, we calculate the local density of states (LDOS) for evaluating the stability and controllability of MCMs in non-square superconducting islands. In Sec. IV, the differential conductance of normal lead wire/noncentrosymmetric superconductor hybrids is calculated by using lattice Green's function techniques. We demonstrate that the zero-bias conductance shows the periodicity as a function of the direction of the applied magnetic field, which serves as a fingerprint of the controllable MCMs. Our conclusion is given in Sec. V.

II. EDGE THEORY AND TUNABLE MAJORANA CORNER MODES

A. Model

Let us consider a two-dimensional noncentrosymmetric $(s+p)$ -wave superconductor in the presence of an in-plane magnetic field. We start with a Bogoliubov-de Gennes (BdG) Hamiltonian in momentum space [66–68],

$$\tilde{H}(\mathbf{k}) = \tilde{H}_{\text{ncs}}(\mathbf{k}) + \tilde{H}_Z \quad (1)$$

with

$$\tilde{H}_{\text{ncs}}(\mathbf{k}) = \begin{bmatrix} \hat{h}(\mathbf{k}) & \hat{\Delta}(\mathbf{k}) \\ -\hat{\Delta}^*(-\mathbf{k}) & -\hat{h}^*(-\mathbf{k}) \end{bmatrix}, \quad (2)$$

$$\hat{h}(\mathbf{k}) = \xi(\mathbf{k})\hat{\sigma}_0 + \lambda \mathbf{g}(\mathbf{k}) \cdot \hat{\boldsymbol{\sigma}}, \quad (3)$$

$$\hat{\Delta}(\mathbf{k}) = [\Delta_s + \mathbf{d}(\mathbf{k}) \cdot \hat{\boldsymbol{\sigma}}] (i\hat{\sigma}_2), \quad (4)$$

$$\xi(\mathbf{k}) = \frac{\hbar^2 k^2}{2m} - \mu, \quad \mathbf{d}(\mathbf{k}) = \Delta_t \frac{\mathbf{g}(\mathbf{k})}{k_F}, \quad (5)$$

and

$$\tilde{H}_Z = \begin{bmatrix} \mathbf{V}_Z \cdot \hat{\boldsymbol{\sigma}} & 0 \\ 0 & -\{\mathbf{V}_Z \cdot \hat{\boldsymbol{\sigma}}\}^* \end{bmatrix}, \quad (6)$$

where m is the effective mass of an electron, μ denotes the chemical potential, $k_F = \sqrt{2m\mu}/\hbar$ represents the Fermi wave number, and $k = \sqrt{k_x^2 + k_y^2}$. The strength of Rashba spin-orbit coupling is given by λ with $\mathbf{g}(\mathbf{k}) = (k_y, -k_x, 0)$. The pair potential $\hat{\Delta}(\mathbf{k})$ contains both a spin-singlet s -wave component Δ_s and a

spin-triplet p -wave component $\mathbf{d}(\mathbf{k})$ satisfying $\mathbf{d}(\mathbf{k}) \parallel \mathbf{g}(\mathbf{k})$ [66]. The Zeeman potential induced by the externally applied in-plane magnetic field is described by $\mathbf{V}_Z = (V_Z \cos \theta_Z, V_Z \sin \theta_Z, 0)$, with θ_Z representing the angle of the magnetic field measured from the x direction. In what follows, without loss of generality, we assume $\lambda, \Delta_s, \Delta_t, V_Z \geq 0$. The Pauli matrices in spin space are given by $\hat{\boldsymbol{\sigma}} = (\hat{\sigma}_x, \hat{\sigma}_y, \hat{\sigma}_z)$, and the 2×2 unit matrix is denoted by σ_0 .

We briefly discuss the topological property of the pure noncentrosymmetric $(s+p)$ -wave superconductor described by $\tilde{H}_{\text{ncs}}(\mathbf{k})$. The positive eigen energies of $\tilde{H}_{\text{ncs}}(\mathbf{k})$ are given by

$$E_{\eta}^{\text{ncs}}(\mathbf{k}) = \sqrt{\{\xi(\mathbf{k}) + \eta\lambda k\}^2 + \{\Delta_t(k/k_F) + \eta\Delta_s\}^2}, \quad (7)$$

with $\eta = \pm$. While the spectrum of $E_{+}^{\text{ncs}}(\mathbf{k})$ has a finite superconducting gap irrespective of the parameters, the superconducting gap in $E_{-}^{\text{ncs}}(\mathbf{k})$ vanishes when

$$\Delta_s = \Delta_c, \quad (8)$$

with

$$\Delta_c = \Delta_t \left[\sqrt{1 + \left(\frac{\lambda k_F}{2\mu} \right)^2} + \frac{\lambda k_F}{2\mu} \right]. \quad (9)$$

For $\Delta_s > \Delta_c$ ($\Delta_s < \Delta_c$), the BdG Hamiltonian $\tilde{H}_{\text{ncs}}(\mathbf{k})$ can be deformed into the BdG Hamiltonian of a pure spin-singlet s -wave (pure spin-triplet helical p -wave) superconductor without any gap closing by decreasing λ and Δ_t (Δ_s) adiabatically. The spin-triplet helical p -wave superconductor is well known as a time-reversal invariant topological superconductor characterized by a \mathbb{Z}_2 topological invariant [74, 75], whereas the spin-singlet superconductor is topologically trivial. Since the topological invariant never changes without gap closing, the noncentrosymmetric $(s+p)$ -wave superconductor with $\Delta_s < \Delta_c$ is topologically equivalent to the spin-triplet helical p -wave superconductor and hosts the topologically protected helical Majorana edge states [57–61]. In what follows, we only focus on the noncentrosymmetric $(s+p)$ -wave superconductor in the topologically nontrivial phase (i.e., $\Delta_s < \Delta_c$).

Then, we discuss the effects of the Zeeman potential against the bulk energy spectrum. Within first-order perturbation theory with respect to V_Z , the energy spectrum is given by

$$E_{\eta}(\mathbf{k}) = E_{\eta}^{\text{ncs}}(\mathbf{k}) + \eta V_Z \sin(\theta_{\mathbf{k}} - \theta_Z), \quad (10)$$

with $\theta_{\mathbf{k}} = \arctan(k_y/k_x)$. Although the Zeeman potential causes a non-monotonic energy shift, it is clear that the Zeeman potential suppresses the superconducting gap size, and a large enough Zeeman potential may bring the system into a gapless superconducting state similar to the case of the pure helical p -wave superconductor discussed in Ref. [76]. Thus, throughout this paper, we only assume weak enough Zeeman potentials,

such that the bulk superconducting gap remains finite and large enough. Although the superconducting gap remains finite, the noncentrosymmetric ($s + p$)-wave superconductor is no longer characterized by the \mathbb{Z}_2 topological invariant due to broken time-reversal symmetry. Nevertheless, in the following, we demonstrate that the noncentrosymmetric ($s + p$)-wave superconductor under the in-plane magnetic field becomes a second-order topological superconductor hosting MCMs.

B. Effective Edge Hamiltonian

In order to discuss the emergence of MCSs in the present system intuitively, we derive an edge theory, similar to the ones discussed in Refs. [41, 43, and 49]. We here assume that the present superconductor has an edge perpendicular to $\mathbf{n} = (\cos \gamma, \sin \gamma, 0)$, where the spatial coordinate along the direction perpendicular (parallel) to the edge is represented by x_\perp (x_\parallel), and the superconductor occupies the entire half-space $x_\perp \leq 0$ (see Fig. 1). In addition, we apply periodic boundary conditions in the direction parallel to the edge (i.e., the direction along the x_\parallel -axis). To obtain an effective edge Hamiltonian, we rewrite the BdG Hamiltonian in momentum space as,

$$\tilde{H}(\mathbf{k}) = \tilde{H}_0(\mathbf{k}) + \tilde{H}_\parallel(\mathbf{k}) + \tilde{H}_Z, \quad (11)$$

$$\tilde{H}_0(\mathbf{k}) = \begin{bmatrix} \hat{h}_0(\mathbf{k}) & \hat{\Delta}_0(\mathbf{k}) \\ -\hat{\Delta}_0^*(-\mathbf{k}) & -\hat{h}_0^*(-\mathbf{k}) \end{bmatrix}, \quad (12)$$

$$\hat{h}_0(\mathbf{k}) = \xi(\mathbf{k}) \left(\frac{\hbar^2 k^2}{2m} - \mu \right) \hat{\sigma}_0 + \lambda k_\perp \hat{\sigma}_\parallel, \quad (13)$$

$$\hat{\Delta}_0(\mathbf{k}) = \left[\Delta_s + \frac{\Delta_t}{k_F} k_\perp \hat{\sigma}_\parallel \right] (i\hat{\sigma}_2), \quad (14)$$

$$\tilde{H}_\parallel(\mathbf{k}) = \begin{bmatrix} \hat{\lambda}_\parallel(k_\parallel) & \hat{\Delta}_\parallel(k_\parallel) \\ -\hat{\Delta}_\parallel^*(-k_\parallel) & -\hat{\lambda}_\parallel^*(-k_\parallel) \end{bmatrix}, \quad (15)$$

$$\hat{\lambda}_\parallel(k_\parallel) = \lambda k_\parallel \hat{\sigma}_\perp, \quad \hat{\Delta}_\parallel(k_\parallel) = \frac{\Delta_t}{k_F} k_\parallel \hat{\sigma}_\perp (i\hat{\sigma}_2), \quad (16)$$

$$\tilde{H}_Z = \begin{bmatrix} V_\perp \hat{\sigma}_\perp + V_\parallel \hat{\sigma}_\parallel & 0 \\ 0 & -\{V_\perp \hat{\sigma}_\perp + V_\parallel \hat{\sigma}_\parallel\}^* \end{bmatrix}, \quad (17)$$

with

$$k_\perp = k_x \cos \gamma + k_y \sin \gamma, \quad (18)$$

$$k_\parallel = -k_x \sin \gamma + k_y \cos \gamma, \quad (19)$$

$$\hat{\sigma}_\perp = \hat{\sigma}_x \cos \gamma + \hat{\sigma}_y \sin \gamma, \quad (20)$$

$$\hat{\sigma}_\parallel = -\hat{\sigma}_x \sin \gamma + \hat{\sigma}_y \cos \gamma, \quad (21)$$

$$V_\perp = V_Z \cos(\theta_Z - \gamma), \quad V_\parallel = V_Z \sin(\theta_Z - \gamma), \quad (22)$$

where k_\perp (k_\parallel) represent the momentum perpendicular (parallel) to the edge of the superconductor. In what follows, we treat $\tilde{H}_\parallel(\mathbf{k})$ and \tilde{H}_Z as the perturbations. This approximation is justified when $k_\parallel/k_F \ll 1$ and when V_Z is significantly smaller than the superconducting gap. Moreover, in the following analysis, we assume $\Delta_s, \Delta_t \ll \lambda k_F, \mu$.

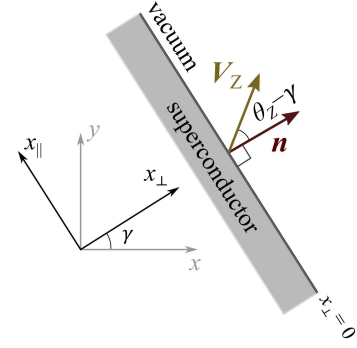


FIG. 1. Edge of the superconductor and relevant spatial coordinates.

For the zeroth-order perturbation, we replace $k_\perp \rightarrow -i\partial_{x_\perp}$ and find zero-energy states satisfying the equation,

$$\tilde{H}_0(-i\partial_{x_\perp}, k_\parallel) \psi(x_\perp) = 0, \quad (23)$$

with the boundary condition $\psi(0) = \psi(-\infty) = 0$. As a result, we find the two solutions,

$$\psi_{+,k_\parallel}(x_\perp) = \frac{1}{2} \begin{bmatrix} e^{-i\gamma/2} \\ ie^{i\gamma/2} \\ -e^{i\gamma/2} \\ -ie^{-i\gamma/2} \end{bmatrix} \varphi_+(x_\perp), \quad (24)$$

$$\psi_{-,k_\parallel}(x_\perp) = \frac{1}{2} \begin{bmatrix} -ie^{-i\gamma/2} \\ -e^{i\gamma/2} \\ ie^{i\gamma/2} \\ e^{-i\gamma/2} \end{bmatrix} \varphi_-(x_\perp), \quad (25)$$

$$\varphi_\zeta(x_\perp) = 2\sqrt{\kappa} \sin(\sqrt{k_F^2 + k_\lambda^2} x_\perp) e^{i\zeta k_\lambda x_\perp} e^{\kappa x_\perp}, \quad (26)$$

$$\kappa = \frac{m\Delta_t}{\hbar^2 k_F}, \quad k_\lambda = \frac{m\lambda}{\hbar^2} \quad (27)$$

with $\zeta = \pm$, where we neglect the insignificant terms of order $O(\frac{k_\parallel^2}{k_F^2}, \frac{\Delta_s}{\mu}, \frac{\Delta_t}{\mu})$. The matrix elements of the perturbation terms $\tilde{H}_\parallel(\mathbf{k}) + \tilde{H}_Z$ within the first order are calculated as

$$a_{\zeta,\zeta'} = \int_{-\infty}^0 dx_\perp \psi_\zeta^\dagger(x_\perp) \{ \tilde{H}_\parallel(\mathbf{k}) + \tilde{H}_Z \} \psi_{\zeta'}(x_\perp). \quad (28)$$

As a result, we obtain an effective edge Hamiltonian,

$$\mathcal{H}' = \begin{bmatrix} a_{+,+} & a_{+,-} \\ a_{-,+} & a_{-,-} \end{bmatrix} = \begin{bmatrix} V_\parallel & \alpha k_\parallel \\ \alpha^* k_\parallel & -V_\parallel \end{bmatrix}, \quad (29)$$

$$\alpha = \frac{\beta(\Delta_t - i\lambda k_F)}{k_F}, \quad \beta = \frac{\Delta_t}{\lambda k_F} \frac{4\mu^2 + (\lambda k_F)^2}{4\mu^2}, \quad (30)$$

which is unitarily equivalent to

$$\mathcal{H} = \begin{bmatrix} \gamma k_\parallel & V_\parallel \\ V_\parallel & -\gamma k_\parallel \end{bmatrix}, \quad (31)$$

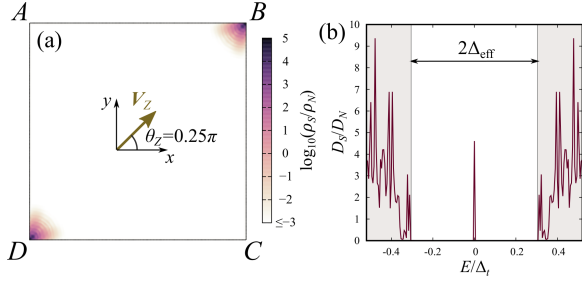


FIG. 2. (a) LDOS at zero energy of the tight-binding model on a square lattice with (201×201) lattice sites. Specifically, we plot the spatial distribution of $\log_{10}(\rho_S/\rho_N)$. The four corners are labeled as A , B , C , and D , respectively. (b) DOS as a function of energy E .

with $\gamma = \beta \sqrt{\Delta_t^2 + (\lambda k_F)^2}/k_F$. From Eq. (31), we clearly find that the mass term for the linearly dispersive helical edge states is given by $V_{\parallel} = V_Z \sin(\theta_Z - \gamma)$. Importantly, the sign of the mass term is determined only by the relative angle between the Zeeman field \mathbf{V}_Z and the edge normal vector \mathbf{n} :

$$\begin{aligned} V_{\parallel} &> 0 & \text{for } 0 < \theta_Z - \gamma < \pi, \\ V_{\parallel} &< 0 & \text{for } -\pi < \theta_Z - \gamma < 0, \\ V_{\parallel} &= 0 & \text{for } \theta_Z - \gamma = 0, \pi. \end{aligned} \quad (32)$$

Thus, there is a possibility that two adjacent edges of the system have the mass terms with opposite signs. In such case, we obtain zero energy states bounded in the vicinity of the corner (i.e., MCMs) because the mass term has a kink there [41, 43, 49]. In the next section, we confirm the validity of our edge theory by performing numerical calculations of a tight-binding model.

C. Tunable Majorana corner modes

We here consider a square superconducting island as shown in Fig. 2(a), where the four corners are labeled as A , B , C , and D , respectively. When we apply the Zeeman field along $\theta_Z = 0.25\pi$, according to Eq. (32), the edges AB and DA have negative mass terms, whereas the edges BC and CD have positive mass terms. Therefore, based on the effective edge theory, we can expect MCMs at the corners B and D . To confirm the above statement, we numerically calculated the LDOS by using the formula $\rho_S(\mathbf{r}, E) = -\text{Tr} [\text{Im} \{ \tilde{G}(\mathbf{r}, \mathbf{r}, E + i\delta) \}] / \pi$, where $\tilde{G}(\mathbf{r}, \mathbf{r}', E)$ represents the Green's function and Tr denotes the trace in spin and Nambu spaces. δ is a small imaginary part added to the energy E . The Green's function is calculated on a tight-binding model by use of a recursive Green's function technique [77], where we replace $\xi(\mathbf{k}) \rightarrow 2t(1 - \cos k_x) + 2t(1 - \cos k_y) - \mu$, $\mathbf{g}(\mathbf{k}) \rightarrow (\sin k_y, -\sin k_x, 0)$, and $\Delta_t/k_F \rightarrow \Delta_t$. The explicit expression of the BdG tight-binding Hamiltonian

is given in Appendix A. In Fig. 2(a), we show the LDOS at zero energy for a (201×201) square island. We use the parameters: $\mu = t$, $\lambda = 0.5t$, $\Delta_t = 0.5t$, $\Delta_s = 0.2\Delta_t$, $V_Z = 0.5\Delta_t$, and $\delta = 10^{-4}\Delta_t$. The LDOS is normalized by $\rho_N = \langle \rho_N(\mathbf{r}, E = 0) \rangle$, where $\rho_N(\mathbf{r}, E)$ representing the LDOS for the normal state (i.e., $\Delta_t = \Delta_s = 0$), and $\langle \dots \rangle$ means the averaged value with respect to the lattice sites. Moreover, we plot $\log_{10}(\rho_S/\rho_N)$ instead of the raw data of ρ_S . As shown in Fig. 2(a), the LDOS at zero energy has a significant amplitude only in the vicinity of the corners B and D . This result confirms the presence of MCMs, as expected. In Fig. 2(b), we show the density of states (DOS) as a function of the energy. The DOS is calculated by $D_S(E) = \sum_{\mathbf{r} \in S} \rho_S(\mathbf{r}, E)$, where $\sum_{\mathbf{r} \in S}$ represents the summation over the lattice sites in the superconductor island. The results are normalized by the DOS in the normal state, $D_N = (201 \times 201)\rho_N$. As shown in Fig. 2(b), the DOS exhibits a sharp zero energy peak inside the superconducting gap $\Delta_{\text{eff}} = 0.31\Delta_t$. Due to particle-hole symmetry of the superconductor, the two MCMs can depart from zero energy only when they hybridize with each other, thereby becoming conventional electron-like and hole-like quasiparticle modes. Therefore, as long as the two MCMs are spatially separated and protected by the superconducting gap Δ_{eff} , they can remain robust at zero energy.

Next, we discuss the controllability of the MCMs. In Fig. 3, we show the LDOS at zero energy with various magnetic field directions, namely (a) $\theta_Z = 0.375\pi$, (b) 0.5π , (c) $0.625\pi/8$, and (d) 0.75π . When $\theta_Z = 0.375\pi$, according to Eq. (32), the kinks of the mass term are located at the corners B and D . As a result, although the spatial distributions of the MCMs are slightly modulated from the case with $\theta_Z = 0.25\pi$, we can still find

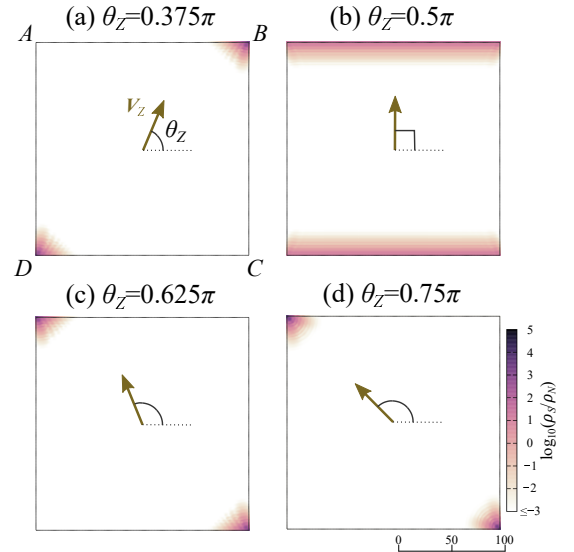


FIG. 3. LDOS at zero energy with (a) $\theta_Z = 3\pi/8$, (b) $\pi/2$, (c) $5\pi/8$, and (d) $3\pi/4$.

them at the corners B and D . When $\theta_Z = 0.5\pi$, the mass term becomes zero at the entire edges AB and CD . As a consequence, zero-energy Majorana *edge* states appear on the entire edges AB and CD . The emergence of Majorana edge states in a time-reversal invariant topological superconductor under a Zeeman field with a certain direction has been discussed in terms of the Majorana Ising spin [59, 78–80], and it has been shown that the energy spectrum of the edge states becomes gapless (strictly speaking, the energy spectrum is discrete due to the finite size effect) [41, 59, 78–80]. When θ_Z exceeds 0.5π , the positions of the mass term kink move to the corner A and C . As a consequence, for $\theta_Z = 0.625\pi$ and 0.75π , the MCMs appear at the corners A and C . By varying the direction of the Zeeman field from $\theta_Z = 0.25\pi$ to 0.75π , the MCM originally located at the corner B hop to the corner A . In the same way, the pair of the MCMs can make a full circle around the system by rotating the direction of the Zeeman field by 2π .

III. EFFECT OF EDGE IMPERFECTIONS

In the above, we have demonstrated that the noncentrosymmetric ($s + p$)-wave superconductor can host tunable MCMs. However, in real experiments, the superconducting island generally deviates from the perfect square shape. Thus, in this section we study the effects of different island shapes (subsection III A) and of edge disorder (subsection III B).

A. Non-square geometry

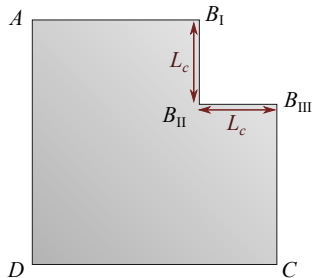


FIG. 4. Non-square island obtained by removing an $(L_c \times L_c)$ square from the upper right corner of a bigger square.

As an example of a non-square shape, we consider a square island, where a square regions of size $(L_c \times L_c)$ has been removed from the upper right corner B [41], as shown in Fig. 4. We label the six corners as A , B_I , B_{II} , B_{III} , C , and D . We first consider the MCMs for a field applied along the direction $\theta_Z = 0.25\pi$. Under this circumstance, according to Eq. (32), the mass term changes its sign at the four corners B_I , B_{II} , B_{III} , and D . In Fig. 5, we show the LDOS at zero energy for an

island with the shape of Fig. 4 with (a) $L_c = 60$ and (b) $L_c = 15$. In accordance with the edge theory, as shown in Fig. 5(a), we find four MCMs for the island with $L_c = 60$. However, for an island with $L_c = 15$, there are only two MCMs, where one of them is spread across the corners B_I , B_{II} , and B_{III} . This implies that the three MCMs originally located at B_I , B_{II} and B_{III} hybridize with each other thereby becoming non-degenerate, with two states at small non-zero energy and one state at zero energy, in accordance with particle-hole symmetry. In fact, the edge theory is valid only when the edges are sufficiently longer than the decay length of the MCMs because, to derive the edge theory, we apply the periodic boundary condition in the direction parallel to the edge and do not take into account the length of the edge. Roughly speaking, the decay length of the MCM is evaluated by the inverse of the superconducting gap [81], i.e., $\xi_{\text{eff}} \approx t/\Delta_{\text{eff}}$, where $\xi_{\text{eff}} = 6.5$ with the present parameter choices. Thus, when L_c exceeds ξ_{eff} significantly, we obtain the MCMs at the three corners B_I , B_{II} and B_{III} . In Fig. 5(c), we show the DOS at zero energy as a function of L_c , where the DOS is normalized by $D_{\text{sq}}(E = 0)$ representing the zero-energy DOS for the ideal square island, calculated in Fig. 2(b). When L_c is large enough (i.e., $L_c \gtrsim 30$), we find $D_S/D_{\text{sq}} = 2$. Although the DOS does not count directly the number of the states, the relation of $D_S/D_{\text{sq}} = 2$ implies that the number of the MCMs in the present island is twice as much as that in the ideal square island: there are four MCMs as shown in Fig. 4(a). For $L_c \lesssim 16$, we find $D_S/D_{\text{sq}} \approx 1$ suggesting the presence of two MCMs as shown in Fig. 4(b). In the intermediate region (i.e. $16 \lesssim L_c \lesssim 30$), the DOS shows non-monotonic oscillations, which originate from interference effects between the three MCMs, which modify their mutual couplings.

In Fig. 6(a), we show the DOS at zero energy as a function of the angle of the Zeeman field, where we vary $0 \leq \theta_Z \leq 0.625\pi$ and choose $L_c = 60$. We find $D_S/D_{\text{sq}} \approx 2$ for $0.1\pi \lesssim \theta_Z \lesssim 0.4\pi$, whereas $D_S/D_{\text{sq}} \approx 1$ for $0 \lesssim \theta_Z \lesssim 0.06\pi$ and $0.45\pi \lesssim \theta_Z$. Therefore, the number of the MCMs changes by rotating the Zeeman potential. To see more details, in Figs. 6(b)-6(i), we present the LDOS at zero energy for eight different values of θ_Z . When $\theta_Z = 0$, as shown in Fig. 6(b), we find the Majorana edge states at the edge $B_{III}C$, whereas there are no significant enhancement in the LDOS at the edge $B_I B_{II}$. When $\theta_Z = 0.03\pi$, as shown in Fig. 6(c), an MCM appears at the corner B_{III} , where the wave function is extended towards the corner C . In addition, we find the small enhancement of the LDOS at the edge $B_I B_{II}$. Strictly speaking, this small enhancement is not originated from exact zero energy states but from the finite energy states having energy extremely close to zero. We cannot eliminate contributions from such low-energy states because, although the strict definition of the LDOS is given by $\rho_S(\mathbf{r}, E) = -\lim_{\delta \rightarrow 0+} \text{Tr} [\text{Im} \{ \hat{G}(\mathbf{r}, \mathbf{r}, E + i\delta) \}] / \pi$, the small imaginary part of δ is always set to be finite in our numerical calculations. As shown in Fig. 6(d), the LDOS

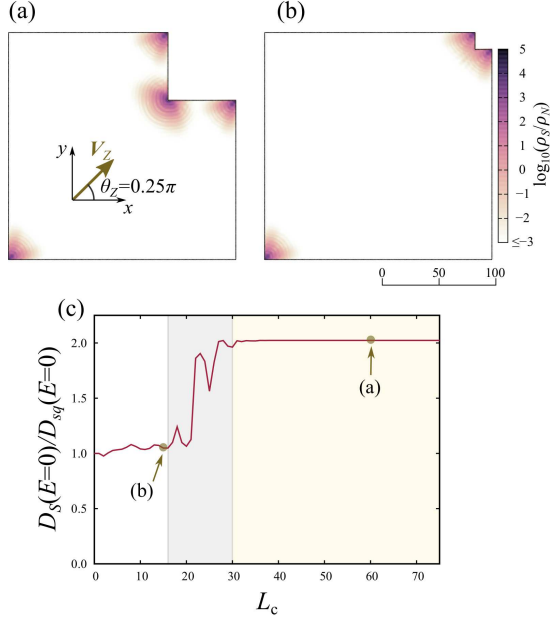


FIG. 5. LDOS at zero energy for the non-square island of Fig. 4 with (a) $L_c = 60$ and (b) $L_c = 15$. In (c), we show the DOS at zero energy as a function of L_c , where the DOS is normalized by $D_{sq}(E = 0)$ representing the DOS of the ideal square island.

at the edge $B_I B_{II}$ increases by increasing θ_Z . When $\theta_Z = 0.1\pi$, as shown in Fig. 6(e), we find that the zero-energy LDOS is significantly enhanced in the vicinity of the corners B_I and B_{II} . As already shown in Fig. 5(a), with $\theta_Z = 0.25\pi$, we obtain three distinct MCMs at the three corners B_I , B_{II} , and B_{III} . As a consequence, by increasing θ_Z from zero to 0.25π , two additional MCMs are created at the corners B_I and B_{II} , while a single MCM stays constantly at the corner B_{II} . When $\theta_Z = 0.4\pi$, as shown in Fig. 6(e), the wave function of the MCM at the corner B_{III} is extended towards the corner B_{II} , such that the MCMs at the corners B_{II} and B_{III} start to overlap with each other. When $\theta_Z = 0.45\pi$, as shown in Fig. 6(e), the LDOS at the edge $B_{II} B_{III}$ is strongly suppressed. With $\theta_Z = 0.5\pi$, we can no longer find the enhancement of the LDOS at the edge $B_{II} B_{III}$, whereas we find a single Majorana edge state at the edge AB_I . With $\theta_Z = 0.625\pi$, we find only two MCMs at the corner A and C . Therefore, by increasing θ_Z from 0.25π to 0.625π , the MCMs at the corner B_{II} and that at B_{III} start to hybridize with each other and move away from zero energy. At the same time the single MCM originally located at the corner B_I hops to the corner A , while the single MCM of corner D hops to corner C . Importantly, in this process, the MCMs originally appearing at B_{II} and B_{III} vanish by hybridizing with each other, and never reappear at any other corner. To accomplish the braiding process in topological quantum computations, we must exchange the positions of the two Majorana zero modes forming a pair. In the present edge configuration,

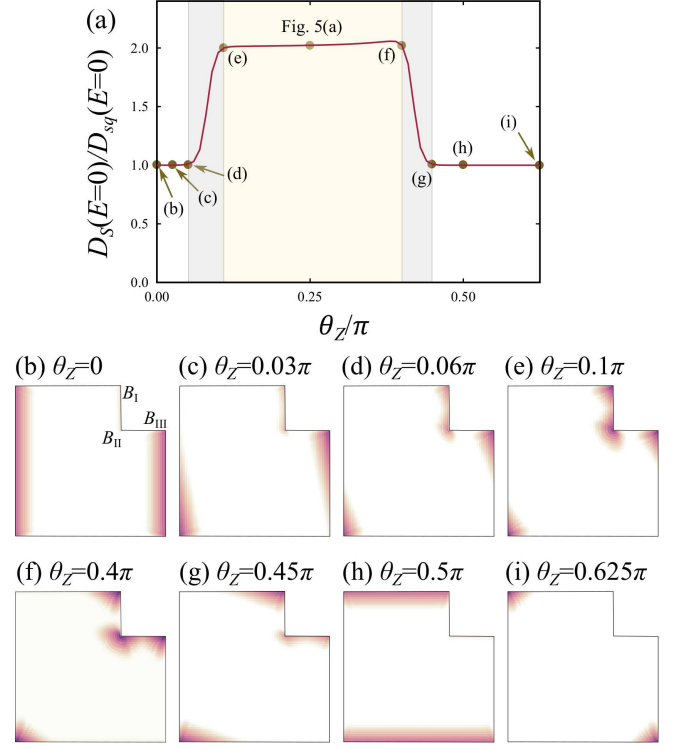


FIG. 6. (a) DOS at zero energy as a function of the angle of the Zeeman field θ_Z , where we choose $L_c = 60$. (b)-(i) LDOS at zero energy for the eight different values of θ_Z indicated in (a).

however, we can no longer find a stable pair of MCMs that can fully circle the edges of the superconductor, and therefore fail the braiding process. To avoid the emergence of additional and undesired MCMs, as also shown in Fig. 5, we have to eliminate additional corners whose adjacent edges are longer than the decay length of the MCMs.

B. Edge roughness

Next, we consider a square island with rough edges. To describe the rough edges, we remove the outermost sites from an ideal square island with probability p , and repeat this etching process X times [82, 83]. With this process, there is a possibility that small debris separated from the largest island are created. Thus, we also remove such debris. In Figs. 7(a) and 7(b), we show the LDOS at zero energy and the DOS as a function of the energy, respectively. We apply the Zeeman field along $\theta_Z = 0.25\pi$ and consider a rough edge with $(p, X) = (0.1, 20)$. We find that the zero-energy LDOS in the vicinity of the corners B and D is enhanced significantly. In addition, as shown in Fig. 7(b), the DOS retains a steep zero energy peak structure, whereas we also find finite DOS inside the effective superconducting gap in the clean limit

$\Delta_{\text{eff}} = 0.31\Delta_t$. As also discussed in Sec. II C, the MCMs are protected by the particle-hole symmetry as long as they are sufficiently separated spatially. Thus, the MCMs remain robust even in the presence of weak or moderate edge roughness that does not destroy the superconducting gap completely.

In Fig. 8(a), we show the normalized DOS at zero energy as a function of the direction of the Zeeman field. For the solid red line, we use the same superconducting island as in Fig. 7(a), i.e., $(p, X) = (0.1, 20)$. For the dotted black line, we consider an island with weaker roughness $(p, X) = (0.1, 5)$. At first, we concentrate on the results with $(p, X) = (0.1, 20)$, shown by the solid-red line. For $0.1\pi \lesssim \theta_Z \lesssim 0.4\pi$ and for $0.69\pi \lesssim \theta_Z \lesssim 0.89\pi$, we find $D_S/D_{\text{sq}} \approx 1$ suggesting the presence of distinct MCMs. However, in the vicinity of $\theta_Z = 0, 0.5\pi$, and π , the DOS shows a non-monotonic dependence and becomes clearly larger than one, i.e., $D_S/D_{\text{sq}} > 1$. To see more details, in Fig. 8(b), we show the LDOS at zero-energy with $\theta_Z = 0.47\pi$, where we use the same superconducting island for calculating the solid-red line in Fig. 8(a). For comparison, in Fig. 8(c), we also show the result with the clean edge. With the dirty edge, we find that the LDOS is enhanced not only in the vicinity of the corner B and D but also around the center of the edge AB and at the corner C . According to the effective edge theory, when θ_Z is close to 0.5π , the mass term $V_{\parallel} = V_Z \sin(\theta_Z - \gamma)$, which is the source of the energy gap in the edge spectrum, is suppressed at the edges AB and CD . Particularly, the mass term of the edges AB and CD vanishes completely at $\theta = 0.5\pi$. The results in Fig. 8 suggest that the already small energy gap is reduced further by the edge roughness, such that states with extremely small (but finite) energy appear at the edges AB and CD . In the topological quantum computations, the energy gap which energetically separates the MCMs from other finite energy states plays an essential role to suppress the decoherence during the braiding operations. Therefore, the edge roughness causing damage to the energy gap in the edge spectrum affects negatively the braiding processes of the MCMs. As shown by the dotted black line in Fig. 8(a), the undesirable enhance-

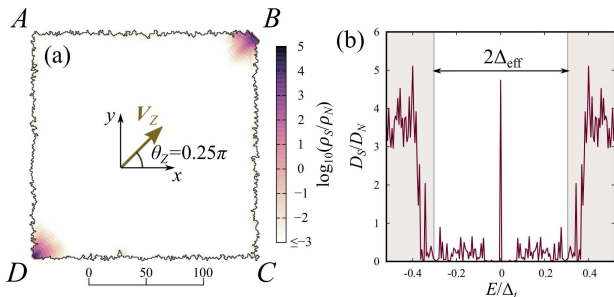


FIG. 7. (a) LDOS at zero energy and (b) DOS as a function of the energy E for the superconducting island with the rough edge $(p, X) = (0.1, 20)$.

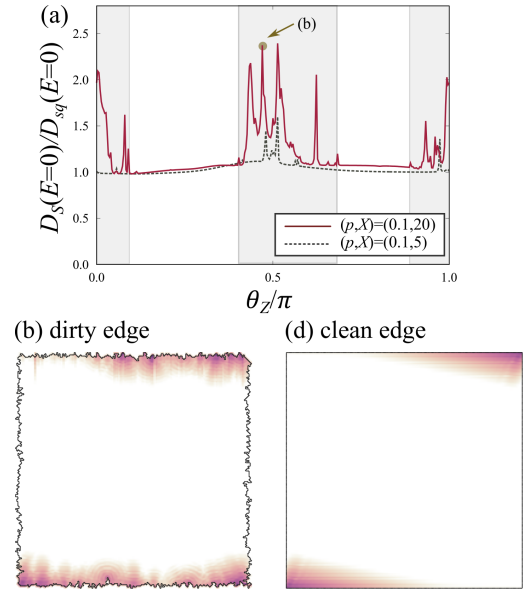


FIG. 8. (a) DOS at zero energy as a function of the angle of the Zeeman field θ_Z . The solid-red line denotes the result with the same island as in Fig. 7(a) [i.e., $(p, X) = (0.1, 20)$], and the dotted black line denotes the result for the island with weaker roughness $(p, X) = (0.1, 5)$. (b)-(c) LDOS at zero energy with $\theta_Z = 0.47\pi$. In (b), we use the same island as in Fig. 7(a) [i.e., $(p, X) = (0.1, 20)$]. In (c), for comparison, we show the result with clean edges.

ment in the low-energy DOS is suppressed by decreasing the edge roughness.

In the above, we have shown that, although the MCMs exist robustly, the braiding operation of them may be disturbed by edge imperfections. The simplest countermeasure would be fabricating superconducting islands with clean and smooth edges. Even so, establishing a practical way to make the braiding process more robust would be a desirable work [52–54].

IV. TUNNELING SPECTROSCOPY

Finally, we propose an experiment for detecting the tunable MCMs. Let us consider a normal lead wire/superconductor junction, where the normal lead wire is attached to a corner of the superconductor as shown in Fig. 9. We describe the present junction with a tight-binding model, where a lattice site is indicated by $\mathbf{r} = j\mathbf{x} + m\mathbf{y}$ with \mathbf{x} (\mathbf{y}) representing the unit vector in the x (y) direction. The superconductor (lead wire) is located at $1 \leq j \leq \infty$ ($-\infty \leq j < 1$) and $1 \leq m \leq W_S$ ($1 \leq m \leq W_N$), where W_S (W_N) denotes the width of the superconductor (lead wire). The superconducting segment is described by the BdG Hamiltonian used also in the above numerical calculations, and the normal lead wire is described by setting $\Delta_t = \Delta_s = 0$ and $\lambda = 0$. The hopping integral between the superconduc-

tor and the lead wire (i.e., $j = 0$ and $j = 1$) is given by t_{int} . The explicit form of the BdG Hamiltonian describing the present junction is given in Appendix A. In the following calculations, we fix the parameters as $\mu = t$, $\lambda = 0.5t$, $\Delta_t = 0.5t$, $\Delta_s = 0.2\Delta_t$, $V_Z = 0.5\Delta_t$, $t_{\text{int}} = 0.1t$, $W_N = 10$, and $W_S = 101$. We assume a sufficiently low transparency at the junction interface (i.e., $t_{\text{int}} = 0.1t$) such that the bias voltage is mainly dropped at the interface. Under this circumstance, we can calculate the differential conductance at zero temperature by using the Blonder–Tinkham–Klapwijk formula [84–86],

$$G(eV) = \frac{e^2}{h} \sum_{\zeta, \zeta'} \left[\delta_{\zeta, \zeta'} - |r_{\zeta, \zeta'}^{ee}|^2 + |r_{\zeta, \zeta'}^{he}|^2 \right]_{E=eV}, \quad (33)$$

where $r_{\zeta, \zeta'}^{ee}$ and $r_{\zeta, \zeta'}^{he}$ denote a normal and Andreev reflection coefficient at energy E , respectively. The indexes ζ and ζ' label an outgoing and incoming channel in the normal lead wire, respectively. These reflection coefficients are calculated using recursive Green's function techniques [77, 87].

In Fig. 10(a), we show the zero-bias conductance $G(eV = 0)$ as a function of the angle of the Zeeman field θ_Z . We find the conductance plateaus at $2e^2/h$ for $0 < \theta_Z < 0.5\pi$ and $\pi < \theta_Z < 1.5\pi$. For these θ_Z , according to the effective edge theory in Sec. II B, the MCM appears at the corner attached to the lead wire. Therefore, it is clear that the conductance plateaus is caused by the resonant tunneling through the MCM. To see more details, in Fig. 10(b)-10(g), we show the differential conductance as a function of the bias voltage for various θ_Z . At $\theta_Z = 0.25\pi$, as shown in Fig. 10(b), we find a steep zero-bias conductance peak, where the conductance spectrum for finite energies displays an almost hard-gap structure. For $\theta_Z = 0.375\pi$, we still find the clear peak, whereas the superconducting gap edge has now a tail that was absent for $\theta_Z = 0.25\pi$. When $\theta_Z = 0.5\pi$, the Majorana *edge* mode appears along the edge perpendicular to the junction interface. Since the Majorana edge mode is not bounded along the junction interface, it cannot cause resonant tunneling [88]. As a result, as shown in Fig. 10(d), the zero-bias conductance peak disappears

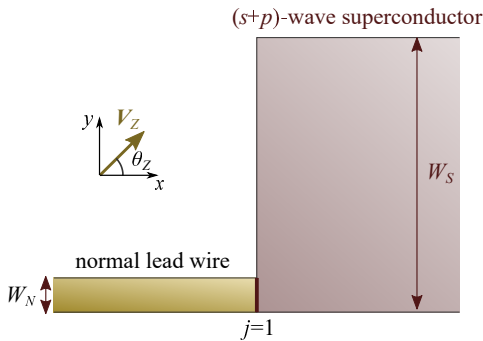


FIG. 9. Schematic image of the normal lead wire/($s+p$)-wave superconductor junction.

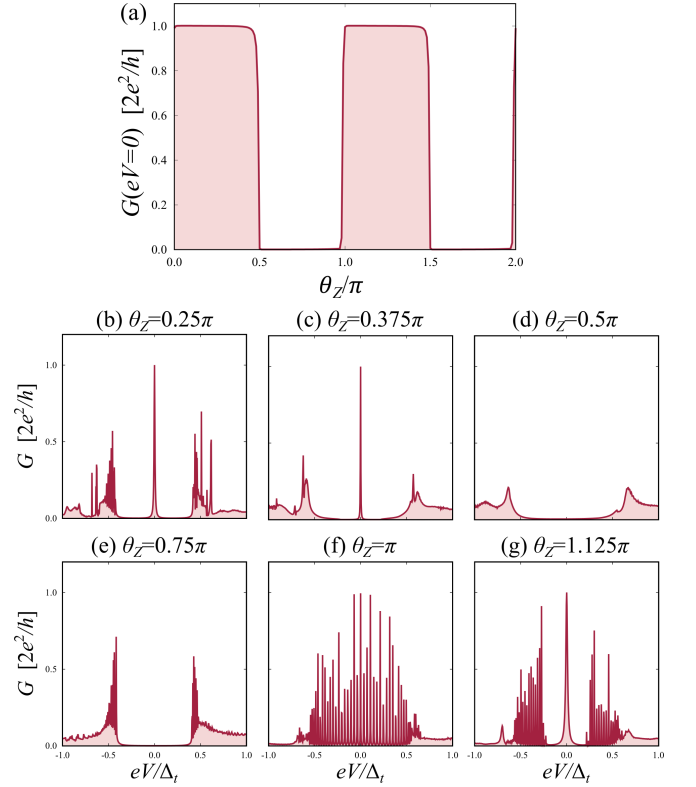


FIG. 10. (a) Zero-bias conductance as a function of the angle of the Zeeman field θ_Z . (b)-(g) Differential conductance as a function of the bias voltages for (b) $\theta_Z = 0.25\pi$, (c) 0.375π , (d) 0.5π , (e) 0.75π , (f) π , and (g) 1.125π .

when $\theta_Z = 0.5\pi$. At $\theta_Z = 0.75\pi$, there are no zero-energy states in the vicinity of the corner attached to the lead wire. As a consequence, we find a hard gap in the conductance spectrum. When $\theta_Z = \pi$, the gapless Majorana edge states appear at the edge along the junction interface. Here, we must note that the energy levels of the Majorana edge states are discretized owing to the finite size of the system. As a consequence, as shown in Fig. 10(f), the conductance spectrum exhibits many spikes for low bias voltages. When we prepare a sufficiently large superconductor, the energy levels of the Majorana edge states will form a continuum, such that the conductance spectra show a broad peak structure instead of a collection of sharp peaks. With $\theta_Z = 1.125\pi$, the MCM again appears at the corner attached to the lead wire. As a consequence, as shown in Fig. 10(g), the conductance spectrum exhibits a zero bias peak, whereas we also find significant enhancement in low bias voltages. When $\theta_Z = 1.25\pi$, the conductance spectrum returns to that in Fig. 10(b).

The periodicity of the zero-bias conductance with respect to the direction of the Zeeman field is a smoking gun evidence for the existence of controllable MCMs. In real experiments, finite temperature effects and other perturbations may modify the details of the conductance

spectrum. Moreover, the edge roughness may disturb the stepwise change in the zero-bias conductance shown in Fig. 10(a) because according to Sec. IIIB, the edge roughness affects significantly the spectrum of the edge states around $\theta = 0, 0.5\pi, \pi$ and 1.5π . Nonetheless, our proposal is still valid for identifying the controllable MCMs because we only need the distinct periodicity in the zero bias conductance, and we do not need any detailed and quantitative informations of the conductance spectrum.

V. CONCLUSION

We have demonstrated that a two-dimensional noncentrosymmetric ($s+p$)-wave superconductor in the presence of an in-plane magnetic field can host tunable Majorana corner modes (MCMs). We also show that the number of MCMs depends sensitively on the edge shape of the noncentrosymmetric superconductor. We find that with irregular edge shapes there are no stable pairs of MCMs that can fully circle around the edges of the superconductor, a property that is important for braiding. We have also studied the effects of edge roughness on the MCMs and found that the MCMs are in general robust to edge roughness. However, edge roughness suppresses the edge gap and may cause undesirable decoherence effects during the braiding process. As a result, although the MCMs can be found insensitive to the edge configurations, the edge imperfections may disturb the realization of topological computations. Therefore, developing practical measures to stabilize the braiding process of tunable MCMs, as well as fabricating clean devices, would be the important future tasks for realizing topo-

logical quantum computations. In addition, we discuss the tunneling spectroscopy in the presence of the MCMs, where a normal lead wire is attached to a corner of the noncentrosymmetric superconductor. The periodicity in the zero-bias conductance with respect to the magnetic field direction is a smoking-gun signature for the existence of controllable MCMs. The proposed experiment is promising for observing the tunable MCMs, because we can expect the periodicity in the zero-bias conductance to be insensitive to the details of the model. In conclusion, we have provided groundwork knowledge for designing specific experiments for detecting tunable MCMs, which is an essential step for realizing future topological quantum computations using higher-order topological superconductors.

ACKNOWLEDGMENTS

This work was supported by the JSPS Core-to-Core program ‘‘Oxide Superspin’’ international network. This research was supported in part by the National Science Foundation under Grant No. NSF PHY-1748958.

Appendix A: Bogoliubov-de Gennes Hamiltonian on a tight-binding model

In this section, we show the explicit form of the BdG Hamiltonian on the tight-binding model. A lattice site is indicated by $\mathbf{r} = j\mathbf{x} + m\mathbf{y}$ with $\mathbf{x}(\mathbf{y})$ representing the unit vector in the x (y) direction. We assume that the superconductor occupies for $1 \leq j \leq L_S$ and $1 \leq m \leq W_S$, and the hard-wall boundary condition is applied in both x and y directions. The BdG Hamiltonian reads $H = H_N + H_\Delta$ with

$$\begin{aligned}
H_N = & -t \sum_{\sigma=\uparrow,\downarrow} \left[\sum_{j=1}^{L_S-1} \sum_{m=1}^{W_S} \left\{ c_{\mathbf{r}+\mathbf{x},\sigma}^\dagger c_{\mathbf{r},\sigma} + c_{\mathbf{r},\sigma}^\dagger c_{\mathbf{r}+\mathbf{x},\sigma} \right\} + \sum_{j=+1}^{L_S} \sum_{m=1}^{W_S-1} \left\{ c_{\mathbf{r}+\mathbf{y},\sigma}^\dagger c_{\mathbf{r},\sigma} + c_{\mathbf{r},\sigma}^\dagger c_{\mathbf{r}+\mathbf{y},\sigma} \right\} \right] \\
& + \sum_{j=1}^{L_S} \sum_{m=1}^{W_S} \sum_{\sigma} (4t - \mu) c_{\mathbf{r},\sigma}^\dagger c_{\mathbf{r},\sigma} \\
& + \frac{i\lambda}{2} \sum_{\sigma,\sigma'} \left[\sum_{j=+1}^{L_S-1} \sum_{m=1}^{W_S} (\hat{\sigma})_{\sigma,\sigma'} \left\{ c_{\mathbf{r}+\mathbf{x},\sigma}^\dagger c_{\mathbf{r},\sigma'} - c_{\mathbf{r},\sigma}^\dagger c_{\mathbf{r}+\mathbf{x},\sigma'} \right\} - \sum_{j=+1}^{L_S} \sum_{m=1}^{W_S-1} (\hat{\sigma}_x)_{\sigma,\sigma'} \left\{ c_{\mathbf{r}+\mathbf{y},\sigma}^\dagger c_{\mathbf{r},\sigma'} - c_{\mathbf{r},\sigma}^\dagger c_{\mathbf{r}+\mathbf{y},\sigma'} \right\} \right] \\
& + \sum_{j=1}^{L_S} \sum_{m=1}^{W_S} \sum_{\sigma,\sigma'} (\mathbf{V}_Z \cdot \hat{\sigma})_{\sigma,\sigma'} c_{\mathbf{r},\sigma}^\dagger c_{\mathbf{r},\sigma'},
\end{aligned} \tag{A1}$$

and

$$\begin{aligned}
H_\Delta = & \frac{i\Delta_t}{4} \sum_{\sigma,\sigma'} \left[-i \sum_{j=+1}^{L_S-1} \sum_{m=1}^{W_S} \delta_{\sigma,\sigma'} \left\{ c_{\mathbf{r}+\mathbf{x},\sigma}^\dagger c_{\mathbf{r},\sigma'}^\dagger - c_{\mathbf{r},\sigma}^\dagger c_{\mathbf{r}+\mathbf{x},\sigma'}^\dagger \right\} - \sum_{j=+1}^{L_S} \sum_{m=1}^{W_S-1} (\hat{\sigma}_z)_{\sigma,\sigma'} \left\{ c_{\mathbf{r}+\mathbf{y},\sigma}^\dagger c_{\mathbf{r},\sigma'}^\dagger - c_{\mathbf{r},\sigma}^\dagger c_{\mathbf{r}+\mathbf{y},\sigma'}^\dagger \right\} \right] \\
& + \sum_{j=1}^{L_S} \sum_{m=1}^{W_S} \Delta_s c_{\mathbf{r},\uparrow}^\dagger c_{\mathbf{r},\downarrow}^\dagger + \text{H.c.},
\end{aligned} \tag{A2}$$

where $c_{\mathbf{r},\sigma}^\dagger$ ($c_{\mathbf{r},\sigma}$) is the creation (annihilation) operator of an electron at \mathbf{r} with spin $\sigma = \uparrow, \downarrow$, t denotes the nearest-neighbor hopping integral, μ is the chemical potential. The strength of the Rashba spin-orbit coupling is represented by λ . The Zeeman potential due to the externally applied in-plane magnetic field is given by $\mathbf{V}_Z = (V_Z \cos \theta_Z, V_Z \sin \theta_Z, 0)$. The spin-singlet s -wave and spin-triplet p -wave pair potentials are denoted with Δ_s and Δ_t , respectively. The Pauli matrices in spin space are given by $\hat{\sigma} = (\hat{\sigma}_x, \hat{\sigma}_y, \hat{\sigma}_z)$. The normal lead wire in Fig. 9 is described by H_N with replacing $L_S \rightarrow -\infty$,

$W_S \rightarrow W_N$ and $\lambda \rightarrow 0$. The coupling between the lead wire and the superconductor is described by

$$H_{\text{int}} = -t_{\text{int}} \sum_{m=1}^{W_N} \sum_{\sigma} \left[c_{j=1,m,\sigma}^\dagger c_{0,m,\sigma} + c_{0,m,\sigma}^\dagger c_{1,m,\sigma} \right], \quad (\text{A3})$$

where t_{int} denotes the hopping integral at the junction interface.

-
- [1] M. Z. Hasan and C. L. Kane, Rev. Mod. Phys. **82**, 3045 (2010).
- [2] X.-L. Qi and S.-C. Zhang, Rev. Mod. Phys. **83**, 1057 (2011).
- [3] Y. Tanaka, M. Sato and N. Nagaosa, J. Phys. Soc. Jpn. **81**, 011013 (2012).
- [4] M. Sato and Y. Ando, Rep. Prog. Phys. **80**, 076501 (2017).
- [5] D. A. Ivanov, Phys. Rev. Lett. **86**, 268 (2001).
- [6] A. Y. Kitaev, Ann. Phys. **303**, 2 (2003).
- [7] C. Nayak, S. H. Simon, A. Stern, M. Freedman, and S. DasSarma, Rev. Mod. Phys. **80**, 1083(2008).
- [8] J. Alicea, Y. Oreg, G. Refael, F. v. Oppen, and M. P. A. S. Fisher, Nat. Phys. **7**, 412(2011).
- [9] S. DasSarma, M. Freedman, and C. Nayak, npj Quantum Information **1**, 15001(2015).
- [10] N. Read and D. Green, Phys. Rev. B **61**, 10267 (2000).
- [11] A. Y. Kitaev, Phys. Usp. **44**, 131 (2001).
- [12] F. Wilczek, Nat. Phys. **5**, 614-618 (2009).
- [13] R. M. Lutchyn, J. D. Sau, and S. DasSarma, Phys. Rev. Lett. **105**, 077001 (2010).
- [14] Y. Oreg, G. Refael, and F. von Oppen, Phys. Rev. Lett. **105**, 177002 (2010).
- [15] V. Mourik, K. Zuo, S. M. Frolov, S. R. Plissard, E. P. A. M. Bakkers, L. P. Kouwenhoven, Science **336**, 1003 (2012).
- [16] M. T. Deng, C. L. Yu, G. Y. Huang, M. Larsson, P. Caroff, and H. Q. Xu, Nano Lett. **12**, 6414 (2012).
- [17] H. Zhang, C.-X. Liu, S. Gazibegovic, D. Xu, J. A. Logan, G. Wang, N. van Loo, J. D. S. Bommer, M. W. A. de Moor, D. Car, R. L. M. Op het Veld, P. J. van Veldhoven, S. Koelling, M. A. Verheijen, M. Pendharkar, D. J. Pennachio, B. Shojaei, J. S. Lee, C. J. Palmstrøm, E. P. A. M. Bakkers, S. D. Sarma, and L. P. Kouwenhoven, Nature **556**, 74-79 (2018).
- [18] F. Pientka, A. Keselman, E. Berg, A. Yacoby, A. Stern, and B. I. Halperin, Phys. Rev. X **7**, 021032 (2017).
- [19] A. Haim and A. Stern, Phys. Rev. Lett. **122**, 126801 (2019).
- [20] F. Setiawan, A. Stern, and E. Berg, Phys. Rev. B **99**, 220506(R) (2019).
- [21] S. Ikegaya, S. Tamura, D. Manske, and Y. Tanaka, Phys. Rev. B **102**, 140505(R) (2020).
- [22] A. Fornieri, A. M. Whiticar, F. Setiawan, E. Portolés, A. C. C. Drachmann, A. Keselman, S. Gronin, C. Thomas, T. Wang, R. Kallagher, G. C. Gardner, E. Berg, M. J. Manfra, A. Stern, C. M. Marcus, and F. Nichele, Nature **569**, 89-92 (2019).
- [23] H. Ren, F. Pientka, S. Hart, A. T. Pierce, M. Kosowsky, L. Lunczer, R. Schlereth, B. Scharf, E. M. Hankiewicz, L. W. Molenkamp, B. I. Halperin, and A. Yacoby, Nature **569**, 93-98 (2019).
- [24] S. Vaitiekėnas, G. W. Winkler, B. van Heck, T. Karzig, M.-T. Deng, K. Flensberg, L. I. Glazman, C. Nayak, P. Krogstrup, R. M. Lutchyn, and C. M. Marcus, Science **367**, eaav3392 (2020).
- [25] T.-P. Choy, J. M. Edge, A. R. Akhmerov, and C. W. J. Beenakker, Phys. Rev. B **84**, 195442 (2011).
- [26] S. Nadj-Perge, I. K. Drozdov, B. A. Bernevig, and A. Yazdani, Phys. Rev. B **88**, 020407(R) (2013).
- [27] S. Nadj-Perge, I. K. Drozdov, J. Li, H. Chen, S. Jeon, J. Seo, A. H. MacDonald, B. A. Bernevig, and A. Yazdani, Science **346**, 602 (2014).
- [28] B. E. Feldman, M. T. Randeria, J. Li, S. Jeon, Y. Xie, Z. Wang, I. K. Drozdov, B. A. Bernevig, and A. Yazdani, Nat. Phys. **13**, 286 (2017).
- [29] L. Fu and C. L. Kane, Phys. Rev. Lett. **100**, 096407 (2008).
- [30] D. Wang, L. Kong, P. Fan, H. Chen, S. Zhu, W. Liu, L. Cao, Y. Sun, S. Du, J. Schneeloch, R. Zhong, G. Gu, L. Fu, H. Ding, and H.-J. Gao, Science **362**, eaao1797096407 (2018).
- [31] S. Sasaki, M. Kriener, K. Segawa, K. Yada, Y. Tanaka, M. Sato, and Y. Ando, Phys. Rev. Lett. **107**, 217001 (2011).
- [32] A. Yamakage, K. Yada, M. Sato, and Y. Tanaka, Phys. Rev. B **85**, 180509(R) (2012).
- [33] X.-L. Qi, T. L. Hughes, and S.-C. Zhang, Phys. Rev. B **82**, 184516 (2010).
- [34] Q. L. He, L. Pan, A. L. Stern, E. C. Burks, X. Che, G. Yin, J. Wang, B. Lian, Q. Zhou, E. S. Choi, K. Murata, X. Kou, Z. Chen, T. Nie, Q. Shao, Y. Fan, S.-C. Zhang, K. Liu, J. Xia, and K. L. Wang, Science **357**, 294 (2017).
- [35] R.-J. Slager, L. Rademaker, J. Zaanen, and L. Balents, Phys. Rev. B **92**, 085126 (2015).
- [36] W. A. Benalcazar, J. C. Y. Teo, and T. L. Hughes, Phys. Rev. B **89**, 224503 (2014).
- [37] Z. Song, Z. Fang, and C. Fang, Phys. Rev. Lett. **119**, 246402 (2017).
- [38] J. Langbehn, Y. Peng, L. Trifunovic, F. vonOppen, and P. W. Brouwer, Phys. Rev. Lett. **119**, 246401 (2017).
- [39] E. Khalaf, Phys. Rev. B **97**, 205136 (2018).
- [40] Y. Wang, M. Lin, and T. L. Hughes, Phys. Rev. B **98**, 165144 (2018).

- [41] Z. Yan, F. Song, and Z. Wang, Phys. Rev. Lett. **121**, 096803 (2018).
- [42] Q. Wang, C.-C. Liu, Y.-M. Lu, and F. Zhang, Phys. Rev. Lett. **121**, 186801 (2018).
- [43] T. Liu, J. J. He, and F. Nori, Phys. Rev. B **98**, 245413 (2018).
- [44] X. Zhu, Phys. Rev. Lett. **122**, 236401 (2019).
- [45] R.-X. Zhang, W. S. Cole, X. Wu, and S. DasSarma, Phys. Rev. Lett. **123**, 167001 (2019).
- [46] Z. Yan, Phys. Rev. Lett. **123**, 177001 (2019).
- [47] Y.-J. Wu, J. Hou, Y.-M. Li, X.-W. Luo, X. Shi, and C. Zhang, Phys. Rev. Lett. **124**, 227001 (2020).
- [48] G. E. Volovik, JETP Lett. **91**, 201 (2010).
- [49] X. Zhu, Phys. Rev. B **97**, 205134 (2018).
- [50] Y. Volpez, D. Loss, and J. Klinovaja, Phys. Rev. Lett. **122**, 126402 (2019).
- [51] X. Wu, X. Liu, R. Thomale, C.-X. Liu, arXiv: 1905.10648.
- [52] S.-B. Zhang, W. B. Rui, A. Calzona, S.-J. Choi, A. P. Schnyder, and B. Trauzettel, Phys. Rev. Research **2**, 043025 (2020).
- [53] T. E. Pahomi, M. Sigrist, and A. A. Soluyanov, Phys. Rev. Research **2**, 032068(R) (2020).
- [54] S.-B. Zhang, A. Calzona, and B. Trauzettel, Phys. Rev. B **102**, 100503(R) (2020).
- [55] S. Fujimoto, J. Phys. Soc. Jpn. **76**, 051008 (2007).
- [56] M. Smidman, M. B. Salamon, H. Q. Yuan, and D. F. Agterberg, Rep. Prog. Phys. **80**, 036501 (2017).
- [57] C. Iniotakis, N. Hayashi, Y. Sawa, T. Yokoyama, U. May, Y. Tanaka, and M. Sigrist, Phys. Rev. B **76**, 012501 (2007).
- [58] Y. Tanaka, T. Yokoyama, A. V. Balatsky, and N. Nagaosa, Phys. Rev. B **79**, 060505(R) (2009).
- [59] M. Sato and S. Fujimoto, Phys. Rev. B **79**, 094504 (2009).
- [60] Y. Tanaka, Y. Mizuno, T. Yokoyama, K. Yada, and M. Sato, Phys. Rev. Lett. **105**, 097002 (2010).
- [61] A. P. Schnyder and P. M. Brydon, J. Phys.: Condens. Matter **27**, 243201 (2015).
- [62] E. Bauer, G. Hilscher, H. Michor, Ch. Paul, E. W. Scheidt, A. Griбанov, Yu. Seropugin, H. Noël, M. Sigrist, and P. Rogl, Phys. Rev. Lett. **92**, 027003 (2004).
- [63] K. Izawa, Y. Kasahara, Y. Matsuda, K. Behnia, T. Yasuda, R. Settai, and Y. Onuki, Phys. Rev. Lett. **94**, 197002 (2005).
- [64] I. Bonalde, W. Brämer-Escamilla, and E. Bauer, Phys. Rev. Lett. **94**, 207002 (2005).
- [65] H. Mukuda, S. Nishide, A. Harada, K. Iwasaki, M. Yogi, M. Yamashita, Y. Kitaoka, M. Tsujino, T. Takeuchi, R. Settai, Y. Ōnuki, E. Bauer, K. M. Itoh, and E. E. Haller, J. Phys. Soc. Jpn. **78**, 014705 (2009).
- [66] P. A. Frigeri, D. F. Agterberg, A. Koga, and M. Sigrist, Phys. Rev. Lett. **92**, 097001 (2004).
- [67] S. Fujimoto, Phys. Rev. B **72**, 024515 (2005).
- [68] N. Hayashi, K. Wakabayashi, P. A. Frigeri, and M. Sigrist, Phys. Rev. B **73**, 092508 (2006).
- [69] Y. Yanase, and M. Sigrist, J. Phys. Soc. Jpn. **77**, 124711 (2008).
- [70] N. Kimura, K. Ito, H. Aoki, S. Uji, and T. Terashima, Phys. Rev. Lett. **98**, 197001 (2007).
- [71] H. Mukuda, T. Fujii, T. Ohara, A. Harada, M. Yashima, Y. Kitaoka, Y. Okuda, R. Settai, and Y. Onuki, Phys. Rev. Lett. **100**, 107003 (2008).
- [72] Y. Tada, N. Kawakami, and S. Fujimoto, J. Phys. Soc. Jpn. **77**, 054707 (2008).
- [73] T. Takimoto, and P. Thalmeier, J. Phys. Soc. Jpn. **78**, 103703 (2009).
- [74] A. P. Schnyder, S. Ryu, A. Furusaki, A. W. W. Ludwig, Phys. Rev. B **78**, 195125 (2008).
- [75] X.-L. Qi, T. L. Hughes, S. Raghu, and S.-C. Zhang, Phys. Rev. Lett. **102**, 187001 (2009).
- [76] C. L. M. Wong, J. Liu, K. T. Law, and P. A. Lee, Phys. Rev. B **88**, 060504(R) (2013).
- [77] P. A. Lee and D. S. Fisher, Phys. Rev. Lett. **47**, 882 (1981).
- [78] S. B. Chung and S.-C. Zhang, Phys. Rev. Lett. **103**, 235301 (2009).
- [79] R. Shindou, A. Furusaki, and N. Nagaosa, Phys. Rev. B **82**, 180505(R) (2010).
- [80] Y. Xiong, A. Yamakage, S. Kobayashi, M. Sato, and Y. Tanaka, Crystals **7**, 58 (2017).
- [81] A. C. Potter and P. A. Lee, Phys. Rev. Lett. **105**, 227003 (2010).
- [82] M. Wimmer, A. R. Akhmerov, and F. Guinea, Phys. Rev. B **82**, 045409 (2010).
- [83] R. Queiroz and A. P. Schnyder, Phys. Rev. B **89**, 054501 (2014).
- [84] G. E. Blonder, M. Tinkham, and T. M. Klapwijk, Phys. Rev. B **25**, 4515 (1982).
- [85] C. Bruder, Phys. Rev. B **41**, 4017 (1990).
- [86] S. Kashiwaya and Y. Tanaka, Rep. Prog. Phys. **63**, 1641 (2000).
- [87] T. Ando, Phys. Rev. B **44**, 8017 (1991).
- [88] Y. Asano, Y. Tanaka, and S. Kashiwaya, Phys. Rev. B **69**, 134501 (2004).